Transverse instabilities of uprising planar jets formed by wave impacts on vertical walls

PROCEEDINGS A

rspa.royalsocietypublishing.org

Research

Article submitted to journal

Subject Areas:
Fluid Mechanics, Wave Motion, Ocean Engineering

Keywords:
flip-through, wave impact, rim-sheet stability, capillary dynamics

Author for correspondence:
Yasunori Watanabe
e-mail: yasunori@eng.hokudai.ac.jp

Transverse instabilities of ascending planar jets formed by wave impacts on vertical walls

Y. Watanabe[1] and D. M. Ingram[2]

[1]Hokkaido University, Graduate School of Engineering, North 13 West 8, Sapporo, Japan
[2]The University of Edinburgh, School of Engineering, The King's Buildings, Edinburgh, UK

When a steep breaking wave hits a vertical sea wall, in shallow water, a rapidly ascending planar jet forms. This jet is ejected with high acceleration due to pressure created by the violent wave impact on the wall, creating a so-called 'flip-through' event. Previous studies have focussed on the impulsive pressures on, and within, the wall and on the velocity of the jet. Here, in contrast, we consider the formation and break-up of the jet itself. Experiments show that during flip-through a fluid sheet, bounded by a rim, forms. This sheet has unstable transitional behaviours and organising jets; undulations in the thickness of the fluid sheet are rapidly amplified and ruptured into an array of vertical ligaments. Lateral undulations of the rim lead to the formation of finger-jets, which subsequently break up to form droplets and spray. We present, a linear stability analysis of the rim-sheet systems that highlights the contributions of rim retraction and sheet stretching to the breakup process. The mechanisms for the sequential surface deformations in the rim-sheet system are also described. Multiple, distinct, instability modes are identified during the rim deceleration, sheet stretch attenuation and rim retraction processes. The wave numbers (and deformation length scales) associated with these instability modes are shown to lead to the characteristic double peak spectrum of surface displacement observed in the experiments. These mechanisms help to explain the columnar structures often seen in photographs of violent wave impacts on harbour walls.

THE ROYAL SOCIETY PUBLISHING

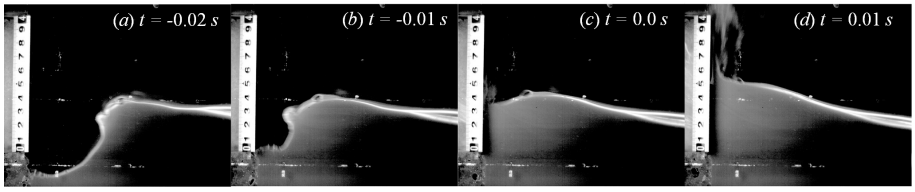

Figure 1. Sequential side view images at flip-through; a breaking wave face hits the vertical wall (wall surface is located at the right edge of the ruler) at phase (c), immediately producing a vertical jet at the impact (time interval of 10 ms). The instant when the forefront of the incident wave touches the wall is defined to be $t = 0.0$s.

1. Introduction

When a shoaling wave crest approaches a vertical wall, the wall prevents the forward flow of water causing the water level at the wall to rise rapidly. The surface between the rising wave trough and advancing crest converges rapidly, and often focus at a point on the wall (see figure 1), resulting in violent wave impact – the so-called flip-through event [1,2]. The thin film-like vertical jet formed at the flip-through is projected upward at high acceleration [3].

In engineering, most attention on this wave–wall interaction has concentrated on the impact pressures acting on the wall during either sloshing impacts [3] or breaking wave impacts [4,5]. The pressure impulse during the flip-through impact has been derived theoretically by Cooker and Peregrine [1,2], providing a mathematical interpretation of underlying dynamics before the start of uprush.

The normal theoretical description assumes both potential flow and homogeneity along the wall, allowing the problem to be simplified by removing the third, transverse, coordinate direction [4]. We have found, however, that the high pressure gradient along the wall, resulting from the impact, accelerates the fluid vertically ejecting a planar thin jet, which follows with inherent transverse deformations (see figure 2 and the supplementary movie file, Movie 1); a horizontal straight rim initially forms along the free edge of the planar jet and subsequently evolves cusp-like formations with simultaneous undulations in the thickness of the film bounded by the rim. The undulations in the rim are rapidly amplified to produce typical finger-shaped jets on the rim as the sheet ruptures. The finger jets are then fragmented into large numbers of droplets forming a spray. The formations of sea spray observed during wave impacts on sea walls may be interpreted using the unstable behaviours of these uprising jets. Such an interpretation is presented here for the first time.

The free-surface dynamics through fingering and breaking up processes have been observed in breaking ocean waves, crown splash and liquid sheet fragmentation.

(a) Breaking waves on beaches

On shallow water coasts (without walls), depth-induced breaking waves have been also found to produce secondary finger jets which are fragmented into droplets at wave splashes. When a breaking wave crest overturns and impacts onto a forward water surface, a secondary jet is rapidly formed and is projected forwards. The initial, two-dimensional, spanwise vorticity produced along the inner surface of the overturning jet becomes unstable and the change in orientation results in multiple pairs of counter-rotating vortices that are stretched obliquely downward beneath the surfaces of the secondary jet [6]. The surface just above these vortex pairs is entrained into the interior of the water to create a convergent free surface flow, resulting in the formation of a transverse array of longitudinal scars on the wave surfaces [7]. In the secondary jet stretching causes the counter-rotating vortices to be intensified within the jet, thus the vortex-induced scars on the jet surfaces are deepened and finally penetrate the jet forming multiple finger jets [8]. The fingers are stretched along the jet axes, breaking up into droplets via

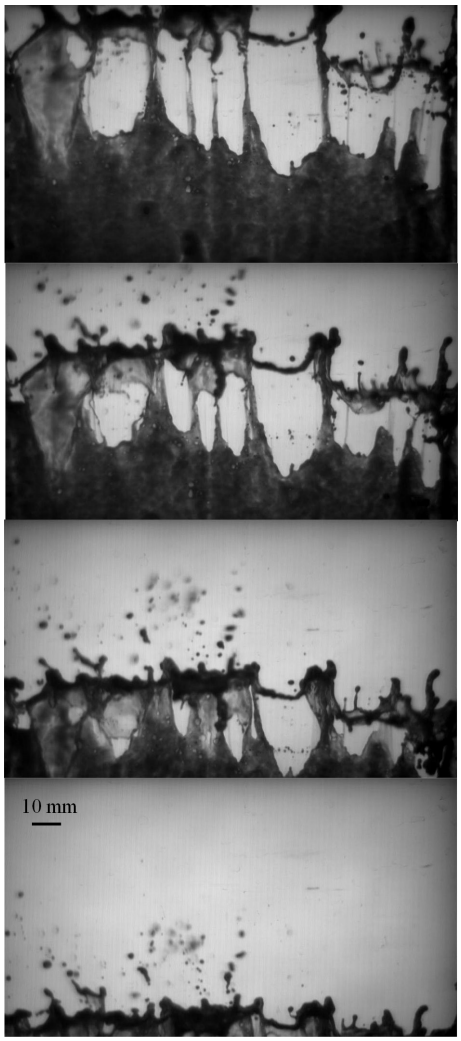

Figure 2. Sequential lateral view images of surface deformations of the flip-through jet at the level of 150 mm above a still water surface. Successive frames (with a 160 mm$\times$90 mm field-of-view), separated by a constant time increment of 4.0 ms, are arranged vertically with the earliest frame at the bottom.

capillary instability. A series of these studies concludes that the initial shear instability manifested in breaking waves triggers the transverse deformation of the jet, evolving into the fingers via vorticity dynamics.

(b) Crown splashes

Crown splashes are also known to produce fingers on an undulating circular rim as a result capillary instability during the retracting behaviour of the rim (see the review by [9]). In this event, a droplet impact initially induces a cavity on receiving liquid and a circular fluid sheet rising with rapid expansion. A circular rim formed along the upper edge of the sheet is pulled back by surface tension during the retracting process. The volume of the rim increases until unstable undulations in the rim grow sufficiently causing the crown structure with the finger jets aligned along the rim. Many investigations of the unstable motion of the rim and the initiation of finger jets have been

performed [10–12] and of the unsteady behaviour of the stretching rim [13,14]. The recent study by Agbaglah et al. [12] concludes that retracting behaviour initially governs the rim instability for short duration in the Rayleigh-Plateau (RP) mode, then Rayleigh-Taylor (RT) instability starts to contribute as the fingers are initiated.

(c) Liquid sheets

Capillary sheet dynamics have been widely studied since theoretical interpretations of the free edge and radically expanding sheet by Taylor [15,16]. Mechanisms for the atomisation of the sheet through a combination of interactive capillary, rim and centrifugal dynamics have been investigated for more complex rim-sheet system [17,18]. Bremond et al. [18] found that the capillary waves traveling on the sheet to the free edge induce amplification of the transverse thickness modulations, leading to the formation of ligaments perpendicular to the sheet edge. Yarin and Weiss [19] show the formation of a cusp-shaped rim is due to capillary discontinuity waves propagating on the sheet.

Strong stretching of the planar jet is known to modify the capillary response. Longuet-Higgins [20] presented another possible mechanism for the longitudinal disintegration of pre-splash overturning jets via modification of the capillary orientation in stretched jet surfaces; capillary waves with transverse crests emerged on a curved free-falling overturning jet. Change in orientation by gravity-induced stretch amplifies the capillary amplitude, causing the lateral disintegration of the falling jet.

These previous findings for breaking waves on beaches, crown splashes and thin liquid sheets provide theories for the dynamics of the flip-through jets induced by wave impacts on vertical walls. In this study, the mechanical and geometrical features of the finger and ligament formations on the uprushing jet are experimentally characterised using these analogies. The mechanical stability of the flip-through jets is also considered using a linear stability analysis for the rim-sheet coupled system using a long wave approximation, and comparisons with the experimental results are made.

The paper is organised as follows. In Section 2, the experimental setup and conditions are explained. Section 3 discusses the geometric features of the deformations of the rim and sheet observed experimentally following the wave impact. In Section 4, the unstable behaviour of the rim-sheet system is discussed, using linear stability analysis, as a model for the jet formed at flip through. Section 5 explains the observed mechanisms to deform the jets during the flip-through event in terms of the transitional instabilities amplified on the system. Finally, the results are summarised in Section 6.

2. Laboratory Experiment

In this section, we explain the measurement system set-up for the water wave experiments comprising: a laboratory wave flume with the vertical wall; an optical system with a high-speed camera; and the wave measurement and control system.

The experiments were performed in a 24 m long wave flume, with a width of 0.6 m and depth of 1.0 m, fitted with a piston type wave maker with active wave absorption. A transparent, acrylic, rectangular, box 0.2 m long and 0.6 m wide with a height of 1.0 m was installed on the 1/20 slope beach to form a breakwater with a vertical seaward face (see figure 3). The static contact angle of the front wall surface with water surface was about 70 ^{o}. The model breakwater was weighted and anchored to the beach to achieving a stationary wall. We define the coordinate system for the experiment with the origin at the point of wave breaking in the horizontal shoreward x axis, the nearside of the flume in the transverse, y, axis and at the still water level in the vertical z axis. The still water depth at the origin $x = 0$ was 100 mm.

The resulting wave impact pressure is very sensitive to the incident wave shape at the impact [4], and consequently the surface behaviour of the vertical jets also depends strongly on the surface shape of the wave face (or local wave steepness). In general, progressive waves with mild

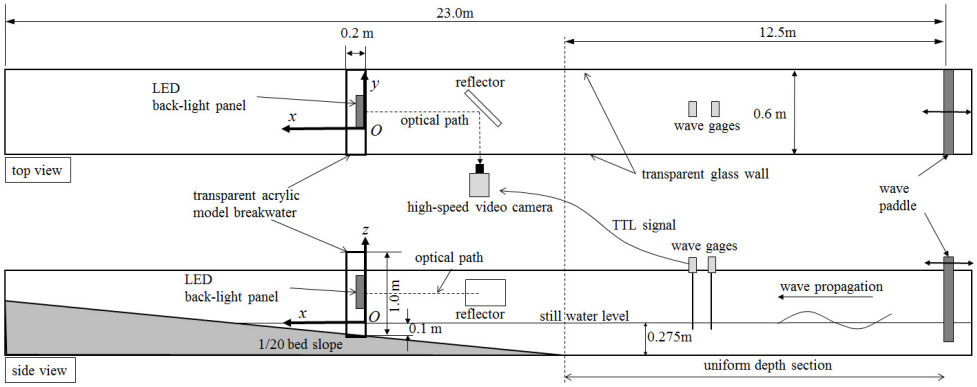

Figure 3. Experimental setup

steepness reflect off the wall and behave like standing waves at the wall, while steeper waves produce more violent impacts causing highly accelerated thin up-rushing fluid jets. The post breaking wave impact provides more complex fluid flows involving entrained air bubbles and induced turbulence. Therefore, in the experiments, the position of the vertical wall, relative to the breaking point, was taken to be a parameter used to define the impact modes of shoaling waves; During the experiments the model breakwater was located at x = -400, -300, -200, -100 mm (in the pre-breaking region) , 0 mm (for the flip-through mode), and 200 mm (for the post-breaking region).

A rectangular blue light-emitting-diode (LED) panel (200$\times$ 100 mm) was set behind the transparent front wall of the model breakwater and used to illuminate the dyed water passing over it. An 8-bit high-speed video camera recorded the illuminated area using a 45° angled reflector (see figure 3). The region illuminated by the LED panel was also traversed vertically from 50 mm above the still water level to +300 mm at 50 mm intervals to allow the vertical evolution of the jets to be examined. The water in the flume was coloured using Uranine dye (Sodium Fluorescein), to enhance contrast of the liquid region. Uranine excites with blue, 436 nm, light and fluoresces with a green, 530 nm, light. A low-pass optical filter ($\leq$ 450 nm) was fitted to the camera, to eliminate the fluorescent emissions from liquid and allow only the blue component, from the back light, to be recorded. The concentration of the dye, 0.11 $\mathrm{mg\,l^{-1}}$, was chosen to ensure that there would be no light transmission across a 0.25 mm thick fluid film. This set up ensures that the image brightness on the liquid area roughly indicates the thickness of the sheet as the transmitted light intensity through the film proportionally decreases with the film thickness. 8-bit, 1280×1024 pixel images were recorded at 500 Hz with an exposure time of 0.125 ms and stored on a PC connected to the camera as uncompressed bitmaps.

Throughout the experiments monochromatic waves with the incident wave height of 146 mm and a wave period of 1.9 s were used. Two wave gages were installed in the constant depth section of the flume, at water depth h of 275 mm, to determine the incident wave height (see figure 3). When the first wave passed the shoreward wave gage, a TTL signal was sent to the high-speed video camera to start recording, this synchronises the impact phase of each of the 20 trials performed for each experimental case to allow a statistical analysis of the results.

In a post-processing procedure, noise on the acquired images was reduced using median filtering. Image coordinates were transformed to real coordinates using a linear image transformation, providing quantitative measures of the liquid surface on images at 0.10 mm/pixel resolution.

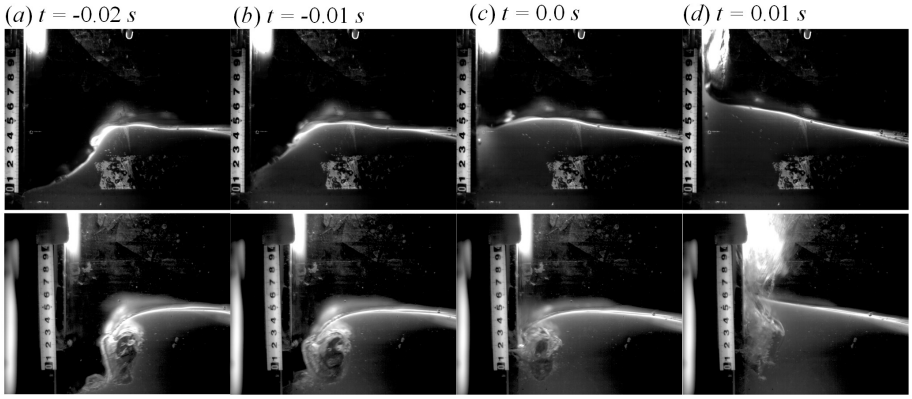

Figure 4. Sequential side view images of surface shapes at the impact at x = -100 mm (top), x = 200 mm (bottom); time interval of 10 ms. The instant when the forefront of the incident wave touches the wall is defined to be $t = 0.0$ s.

3. Experimental results

This section describes the features observed during the experiments in the three impact regimes (pre-breaking, flip-through and post breaking). The transverse deformations of the jets are characterised in terms of wave number spectrum.

(a) Wave impacts

The dynamics of the up-rushing jet depend both on the relative location of the sea wall and the point at which the wave breaks. Clearly, the initial vertical acceleration of the jet resulting from the wave impact depends on the incident wave steepness immediately prior to impact (see detailed in review by [4]). If the wall is far from the breaking zone, linear, sinusoidal waves are reflected by the sea wall forming the characteristic pattern of standing waves. Steeper, shoaling, waves, however, cause rapid changes in dynamic pressure at the wall, accelerating the surface upward during the wave–wall interaction (see phases (a) – (c) on the top panel of figure 4). The vertically accelerated water surface at the wall forms a planar thin film-like jet extending from the standing wave crest as shown in phase (d). In the flip-through case, a nearly vertical wave face progressing toward the wall focuses at a point on the wall with the forward trough lifted up (see phase (c) of figure 1). A high pressure gradient occurring at the focus point ejects the water sheet extending from the standing wave crest (phase (d) of figure 1, and (a) – (d) of figure 5).

In the case of broken wave impact, the overturning jet entraps air prior to impact (see phases (a) and (b) on the bottom panel of figure 4). During the impact, the trapped air is squeezed before finally breaking up into large numbers of bubbles. The resulting aerated water spray is dispersed over a wide area. The entrapped and entrained bubbles significantly change the dynamics of the wave impact; the compressibility of air causes pressure oscillations on the wall and alters the duration of the pressure rise, maximum pressure and the sound speed [4,5]. The combination of these multiple effects of air mixture yields very complex fluid motion in the jet.

Peregrine [21] provided a mathematical model of a splash from a thin layer of water. He interprets the projection of a jet at an angle with respect to the fluid layer by considering the conservation of mass and momentum using Bernoulli's theorem and including both the impact and projections points. The expansion of the crown formed by droplet impacts can be described in terms of the propagation of a discontinuity wave at the projection point on the layer streams [19]. Roisman and Tropea [22] extended this model to derive a solution of the crown shape.

Cooker and Peregrine [2], on the other hand, derived a theoretical solution for the fluid flow in a rectangular wave impact and found that the vertical velocity (v_1) on the free-surface become

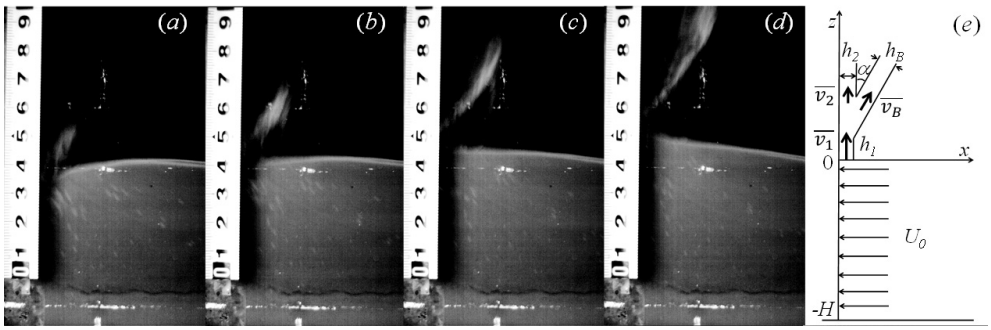

Figure 5. Sequential side view images (a) – (d) of the uprising jet at the flip-through impact; time intervals of 0.002 s, and schematic representation (e) of the formation of the jet from the kinetic discontinuity expected at the flip-thorough impact of a rectangular wave.

infinite at the wall location (x =0); $v_1 \sim -2U_0/\pi \log(x/H)$, where U_0 is the impact velocity normal to the wall and H is the distance from the bottom to the wave crest (see figure 5 e). Assuming that the upward stream in a thin fluid layer, with thickness h_1, on the vertical wall above the free-surface of the rectangular wave occurs at the inception of the impact, despite the singular velocity at the wall, the finite mean velocity may be found by explicitly integrating v_1 over the layer thickness; $\overline{v_1} \sim -2U_0/\pi\,(\log(h_1) - \log(H) - 1)$. Following the approach in Roisman and Tropea [22] for a jet projection from the kinetic discontinuity between the lower and upper layers with thickness ranging from h_1 to h_2 and velocity from $\overline{v_1}$ to $\overline{v_2}$ (see figure 5 e), the mean velocity vector of the jet, $\overline{\boldsymbol{v}_B} \approx (\overline{v_1}\sin\alpha/2, h_1\overline{v_1}/h_B + 4\gamma\cos\alpha/\rho h_B\overline{v_1})$, jet inclination angle $\alpha \approx \arccos\left((h_B - 2h_1)\overline{v_1}^2/(h_B\overline{v_1}^2 - 8\gamma/\rho\right)$, and the jet thickness $h_B = h_1 + h_2$, can be found. In this case of static upper film with $\overline{v_2}$ =0 exists (the impact region on the wall was observed to be wetted by run up of preceding wave and a thin film remains after flip-through impact). Although we are unable to quantify, experimentally, the real thickness of this thin film, assuming the approximate thickness of the projecting jet, $h_B \approx 0.1$ mm (Section 4 (f)) and the thinest lower film of one order thinner than h_B above the free-surface, $h_1 \approx 0.01$ mm, the approximate measures of the mean velocity vector and splash angle are estimated to be $\overline{\boldsymbol{v}_B} \approx (1.3, 6.4)\,\mathrm{ms}^{-1}$, and $\alpha \approx 23^o$, respectively.

Figure 5 (a) – (d) shows the local orientation of the uprising jet formed during the flip-through impact. The jet is ejected upward at angles with respect to the vertical wall that are consistent with the inclination angle approximated by the splash model. This indicates that the uprising fluid moves upward without contacting the wall during the initial jet projection. The flip-through jet may therefore be treat as a free jet.

Figure 6 shows the mean upward velocity of the jet (measured using image analysis) plotted against the location of the wall at three different heights above the still water level. The vertical velocity decreases with increasing height as drag force and gravity decelerates the water sheet. The maximum vertical velocity ($\sim 6.7\mathrm{ms}^{-1}$) occurring at flip-though ($x = 0$) is more than ten times the maximum vertical velocity estimated by the small-amplitude linear wave theory [24] for the standing wave (approximately $0.6\mathrm{ms}^{-1}$). Although an exact comparison of the observed velocity with the analytical predictions of Cooker and Peregrine [2] is impossible because of the singularity at the wall, the predicted mean velocity of the jet is of the same order of the mean velocity of the observed jet. We note that the velocity is also comparable with that reported by Bruce et al. [23] for random wave impacts on a 10:1 battered wall. As the breaking point moves seaward the jet velocity falls off rapidly.

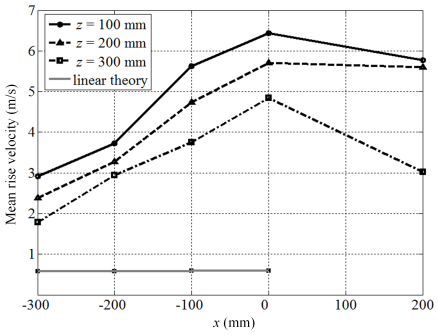

Figure 6. Ensemble mean rise velocities of the jets, and theoretical maximum vertical velocity of the standing wave.

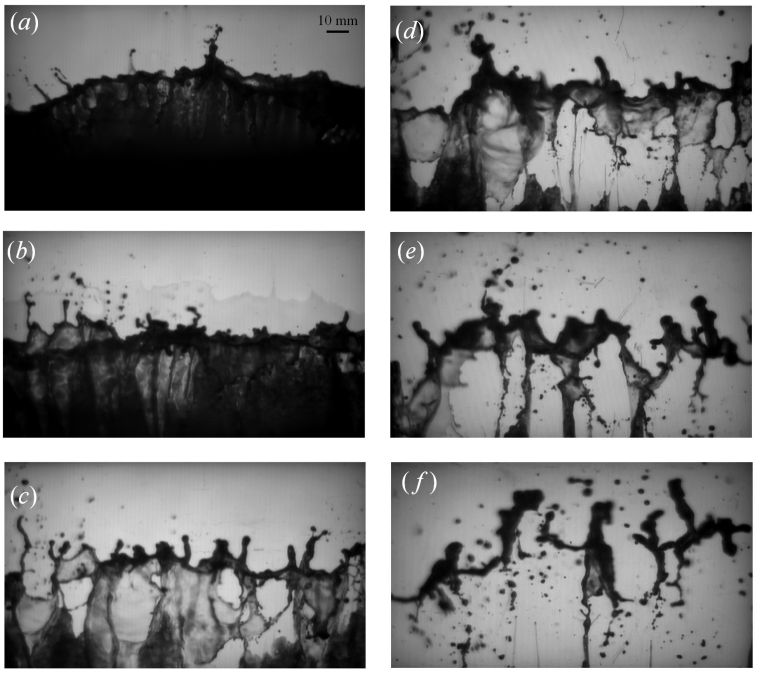

Figure 7. Evolution of transverse surface forms of the flip-through jet via fingering, rupturing film and breakup into sprays; (a) to (f) represent the vertical level z = 50, 100, 150, 200, 250, 300 mm.

(b) Evolution of jets at flip-through

In the experiments no corrugations or irregularities are observed in the wave crest which could lead to transverse changes in velocity during the impact. However, an uneven transverse surface can be observed in the up-rushing sheet together with a defined rim following the impact.

The evolution of the sheet as it initially forms finger jets before rupturing and breaking up into spray is shown in figure 7 (see also the supplementary file, Movie 1). In the early stages of figure 7, images (a) and (b), a rim is observed to form at the leading edge of the sheet-like jet. Image (b) clearly shows a striped pattern bellow the rim, indicating transverse undulations of sheet thickness, these may be due to the capillary re-orientation causing longitudinal disintegration

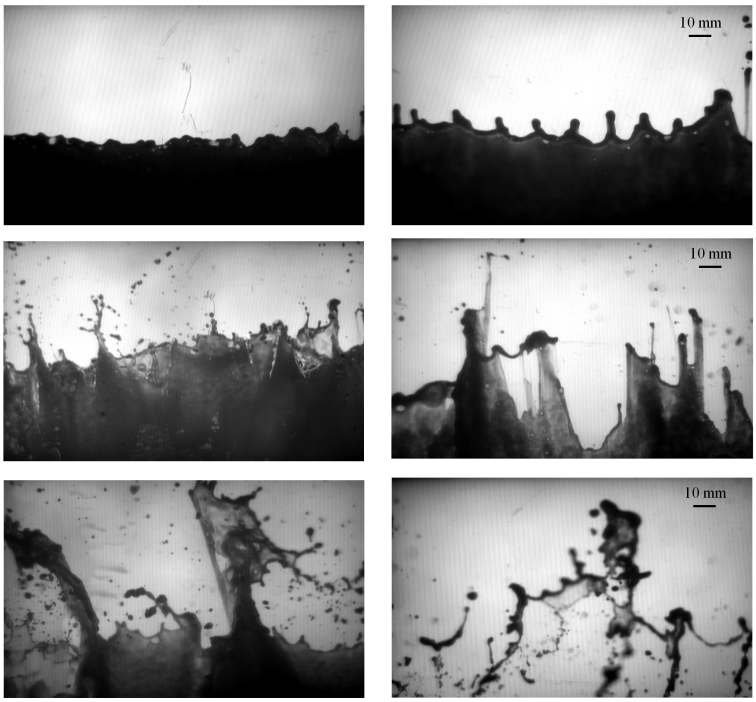

Figure 8. Transverse forms of the tip of uprising jet at x = -200 mm (top, pre-breaking case), x = -100 mm (middle, quasi-flip-through case) and x = 200 mm (post-breaking case); vertical level z = 100 mm (left) and 200 mm (right).

of the thinning jet [20]. As the jet rises (images b to d), the transverse undulations near the rim are amplified forming cusp-like structures before evolving into a regular pattern of finger jets. During this stage of evolution the sheet is being stretched and consequently thins.

The amplified undulations of sheet thickness rupture in the fully stretched sheet, resulting in holes that are then elongated vertically (see images c – d), finally an array of vertical ligaments is formed which merged with the deformed rim (images d – e). The rim-ligament system detaches from the standing wave crest in images (e) to (f), before finally disintegrated into individual droplets through capillary instability. The fact that a wetted wall is not observed after preceding jets have passed in Movie 1 further indicates that their is no contact of the jet with the wall.

Saruwatari et al. [8] found that the mechanism for forming fingers in jets splashing onto a still water is governed by vorticity dynamics within the sheet not by surface tension. They failed to find, however, any evidence of rim formation at either the leading edge of the jet nor the ruptured sheet (as in figure 7), suggesting the mechanisms observed above are different from those for splashing jets. Consequently, vortex dynamics may be irrelevant in the present issue.

The transverse rim instability emerged in the early stages (figure 7 images b to d) is visually analogous to that observed in the crown splash, which may also be interpreted by considering the retracting dynamics and the capillary effect. The regular deformations and breakup of the sheet, formation of the longitudinal ligaments and the detachment of the rim from the sheet have, however, never been reported in crown splashes. The simultaneous amplification of the undulations in sheet thickness, which may be triggered by destabilisation of the stretched, thinning sheet during re-orientation of capillary waves [20], suggests the dynamics of the coupled rim-sheet system governs the breakup mechanism for flip-through jets.

(c) Formation of jets during pre- and post- breaking impacts

Figure 8 shows a series of images of the resulting sheet at $z = 100$ and $200\,\mathrm{mm}$ above the still water level in pre- and post-breaking cases. When the wall is seaward of the breaking point, a standing wave with a uniform transverse wave crest forms. As the wave runs-up on the vertical wall a sheet of water is ejected upwards, which in this case is in contact with the wall. In the top images with the wall $200\,\mathrm{mm}$ seaward of the breaking point, as the sheet emerges small disturbances appear along the edge of the sheet, which are amplified as the sheet stretches to form regular patterns of fingers. In the non-breaking case, where the jet contacts the wall, the shear between the fluid and the wall that also affects the deformation of the jet, which should be treat as a moving contact line problem. Toroian et al. [25] identified unstable transverse behaviour of a spreading film on a slope to interpret the finger formation of the film driven by capillary, gravity and shear balance, which may be relevant to the local deformation of the pre-breaking jet in the deeper water region.

When the wall is closer to the breaking point at $x = -100\,\mathrm{mm}$, a quasi flip-through process is observed (figure 8 middle). In this case a rim with lateral undulations is clearly identifiable on the sheet at $z = 100\,\mathrm{mm}$, while the neck of the jet (associated with the standing wave component) moves up the wall. As the sheet rises, the rim becomes detached from the sheet and ligaments are formed as the sheet ruptures. These features indicate that, in this case, the motion of the preceding sheet can be modeled as a free jet without wall contact.

In the post-breaking case, an air pocket is trapped by the overturning jet and is compressed and collapses into many bubbles when the broken wave hits the wall (see the bottom sequence in figure 4). The aerated fluid forms many very complex and irregular jets, which are dispersed in many directions, as a result of the combined effects of aeration and turbulence (see figure 8 bottom). Large numbers of the spray jets are produced during the initial stage of the impact with some jets evolving into ligaments, which successively breakup into droplets due to the capillary instability. Although it is interesting to discuss the complex fluid motions in this region, many unknown mechanical factors, such as compressibility effects and modifications of pressure responses owing to aeration [4,5], surface-vorticity interactions [8] in addition to the capillary and sheet dynamics, need to be understood for identifying the broken wave impacts, which should be left for future investigations. In this paper, we therefore concentrate on the mechanism of surface deformation and break-up for the flip-through case.

(d) Geometric features of the flip-through jets

In order to quantify the observed deformations of the uprising jets, the edges of liquid areas on the images were detected by an active contour model based on an energy fitting algorithm using a level-set iteration [26]. The detected boundaries for liquid jets and sprays were defined separately; spray droplets are defined as having a closed boundary, while the jet boundary must touch the edge of the image (see figure 9 (a)). Liquid which is out of the focal plane of the camera and which has the maximum absolute gradient of image intensity along the liquid boundaries lower than a given threshold, is removed from ensemble statistics.

An integral length $F(y)$ is useful for quantifying the transverse undulations of the jets. $F(y)$ is defined by counting the pixels in the y^{th} column which are inside a jet (see figure 9), pixels inside spray droplets are explicitly excluded from the count. Figure 9 shows $F(y)$ plotted at three different times, following impact for the flip-though case at z = 100 mm (figure 7 b), the corresponding photographs (a) – (c) are shown above the graph. Although a double-valued surface profile with respect to y may smear $F(y)$ somewhat, we find $F(y)$ consistently defines the transverse locations of the cusped rims and fingers (indicated by broken lines in the sequential images (a) – (c)) and this is used for estimating the major intervals of the rim deformations.

The temporal behaviour of the transverse variations of the integrated lengths are analysed using the Fourier spectrum $S(K)$ to determine the length-scales of the deformations (see figure 10). Here, the dimensional wave number $K = 2\pi/L$ is used where L is the transverse wavelength (in mm). It should be noted that the lowest wave number component, corresponding

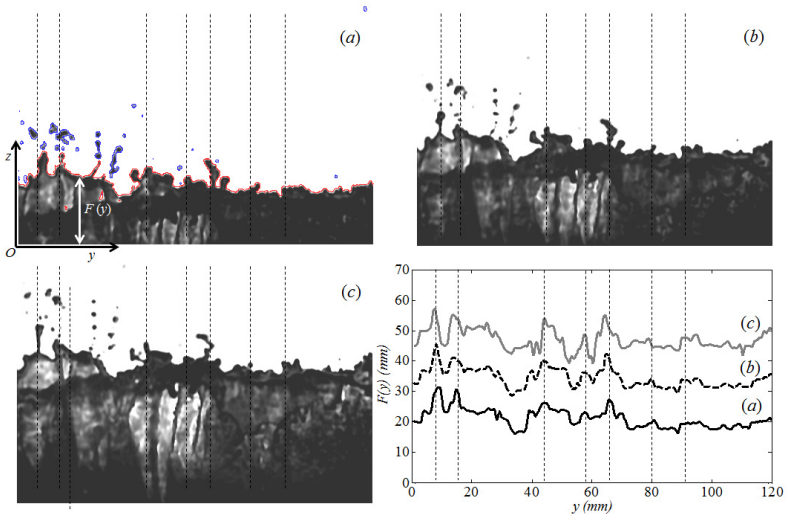

Figure 9. An example of the estimated integrated lengths $F(y)$ for the flip-through jet forms on the sequential images (a) – (c) at z = 100 mm (corresponding level to figure 7 b). The detected interface boundary for the back-light images of the jets (drawn by red lines) and dispersed sprays (blue line) are shown in (a). The broken lines indicate the corresponding locations in the images and plots of $F(y)$.

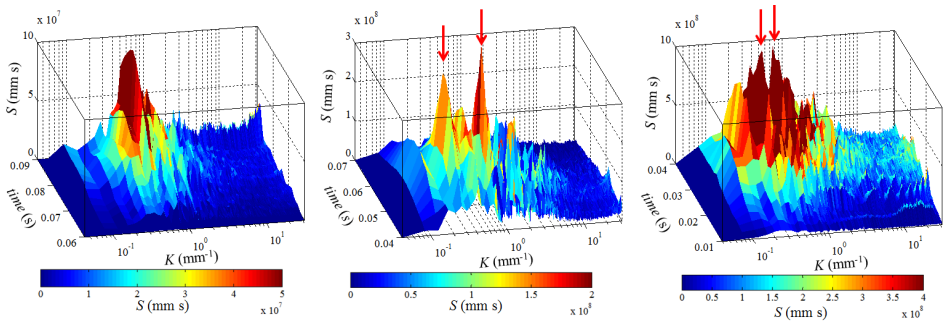

Figure 10. Wave number spectra for the integrated length $F(y)$ at z= 200 mm; x=-200 mm (left), x=-100 mm (middle), x=0 mm (right). Arrows indicate two prominent spectrum peaks observed in quasi-flip-through and flip-through cases.

to the mean surface location, is not shown so as to emphasise higher wave number components. A prominent spectrum band widens as the breaking point approaches, i.e. $x \to 0$. This is a relatively narrow band, $0.3 < K < 1.0$ mm^{-1}, furthest from the breaking point (x = -200 mm) and is widest, $0.1 < K < 2.0$ mm^{-1}, at flip-through (x = 0 mm). At $x = 0$ mm two significant peaks are observed in the spectrum at $K \approx 0.26$ and 0.67 mm^{-1} (corresponding to about 24.2 and 9.4 mm of wavelengths). This suggests two distinctive fluctuation modes triggered by different instability mechanisms govern the formation of the transverse deformations. The observed spectrum is compared later with linear instability growth.

Figure 11 shows a sequence of the mean relative complement image brightness (CIB), averaged over the transverse, y, directions plotted against the z coordinate. As previously discussed (see Section 2) the complement image brightness is proportional to the thickness of the fluid sheet, consequently the $CIB = 1$ if the backlit fluid sheet is thicker than 0.25mm and will be zero where

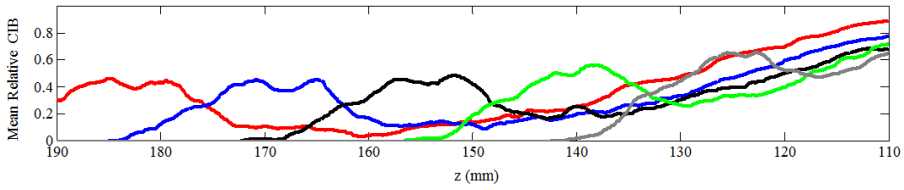

Figure 11. Evolution of transversely averaged relative compliment image brightness of the back-light images taken at z =150 mm. The temporal sequence with time interval of 2.0 ms is indicated by the line color in order of gray, green, black, blue and red.

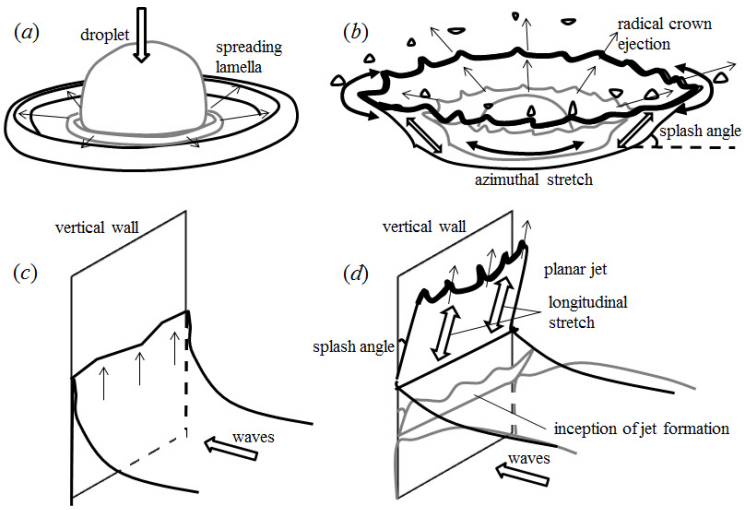

Figure 12. Schematic illustrations of the deposition type of the droplet splash (a), corona splash (b), surface form of the standing wave crest on the vertical wall (c) and the flip-through jet ejected with an inclination angle (d).

there is no fluid in-front of the back light. Figure 11 shows a region of relatively high mean CIB appearing behind the leading edge, due to the presence of the deformed rims, followed by a thiner sheet region, with a correspondingly lower CIB. As the jet rises the sheet, between the wave crest and the rim, elongates and thins. This geometric feature, a thinning sheet with approximately constant thickness, is used as the basis of the rim stability analysis presented in Section 4.

(e) Flip-through vs crown splash

The distinct behaviours of splashing jets, during wave impacts, depend on the relative location of the breaking point and the wall and may be characterised by analogy with droplet impact on a solid wall. Rioboo et al. [27] provide a description of the possible outcomes of droplet impact on a dry wall. The deposition process is characterised, for relatively low impact speed and small droplet size, by a radially spreading lamella which forms during the impacting process (figure 12 a). At higher impact velocity the corona rim and sheet are radically ejected at an inclination angle with respect to the bottom wall (figure 12 b). As the corona (or crown) grows azimuthal stretching and expansion modify the capillary instabilities on the rim [28]. Dropplet impacts on a thin liquid film typically produce identical crown splashes with a specific splash angle [29].

In the case of the splashing jet (figure 12 *c* and *d*), the underlying process can also be split into two distinct types. In the pre-breaking case a laterally uniform planar sheet moves up the vertical wall (see top panel of figure 8 and figure 12 *c*). This type is directly comparable to the deposition type of the droplet impact, but with the thinning sheet spreading upwards rather than radially. In a similar way the flip-through jet can be considered as a planar version of the axisymmetric crown splash. Here the wave impact ejects a fluid sheet, bounded by a rim at an acute angle to the wall (see figures 5 and also 12 d). Unidirectional longitudinal stretching of the sheet results in rapid thinning with transverse undulations. As the sheet stretches these lead to longitudinal ruptures forming a vertical array of ligaments and detachment of the rim from the sheet (figure 7). This mode is never observed in crown splashes with radical expansion. The observation that the unstable behaviour of the rim sheet system is dominated by longitudinal stretching is the basic assumption for the present mathematical model.

(f) Scaling the jet motion

The rim size and the sheet thickness observed in the experiments can be roughly estimated from the back-light image intensity (see Section 2). The rim radius, a_e, is in the range of 1.0 to 1.5 mm during the flip-through event, while the sheet thickness, h_e, just before rupturing is less than 0.1 mm. Consequently, the representative lengths, $a_e \approx 1.0$ mm and $h_e \approx 0.1$ mm have been used for scaling the dynamics of the flip-through jets.

Based on these thicknesses a characteristic velocity and time-scales can be estimated. The retracting behaviour of the sheet is associated with the Taylor-Culick velocity, $v_{ret} = \sqrt{2\gamma/\rho_l h_e}$, which is estimated, using the dimensions from the experiments to be about $1.2\,\mathrm{ms}^{-1}$. Here, ρ_l is the density of liquid and γ is the surface tension. Whilst this is less than the initial velocity of the jet ($\sim 6.7\,\mathrm{ms}^{-1}$, see figure 6) it is of a comparable order of magnitude. The time scale associated with the capillary motion of the sheet is $\tau_{ch} = \sqrt{\rho_l h_e^3/\gamma}$, as the sheet thins and $h_e \to 0$ this time scale becomes shorter, accelerating the capillary behaviour on the sheet. In a similar way the capillary time scale for the rim is $\tau_{cr} = \sqrt{\rho_l a_e^3/\gamma}$, as the rim thickens during the retraction, in contrast with the sheet, the time scale becomes longer and thus the capillary processes on the rim slow down. Based on the experimental measurements these time scales are $\tau_{ch} \approx 1.2 \times 10^{-4}\,\mathrm{s}$ and $\tau_{cr} \approx 3.1 \times 10^{-3}\,\mathrm{s}$. At the initial stage of jet formation the rim and sheet thicknesses are comparable, so consequently $O(\tau_{cr}) \sim O(\tau_{ch})$. With simultaneous onsets of the rim growth and sheet thinning, however, the increasing difference between τ_{cr} and τ_{ch} may lead the sequence of rim and sheet behaviour observed with time lags shown in figure 7. Transverse undulations in the sheet thickness are first observed (figure 7 *a*). As the sheet thins there is rapid growth in these undulations eventually leading to rupture (figure 7 *b* – *c*), while slower transverse deformations of the rim occur for longer duration, eventually leading to fingering (figure 7 *b* – *f*).

The viscous time scales can also be estimated from the experimental measurements; for the sheet, $\tau_{vh} = h_i^2 \nu^{-1} \approx 0.01\,\mathrm{s}$ and for the rim, $\tau_{vr} = a_i^2 \nu^{-1} \approx 1.0\,\mathrm{s}$. Since both these times scales are significantly longer than those associated with the capillary processes we conclude that viscous effects play only a minor roll in the initial unstable motions of the jet. While the effects of viscous shear increase with decreasing thickness, the Ohnesorge numbers for the sheet, $Oh_h = \nu\sqrt{\rho/h_i\gamma} = 0.0117$, and rim, $Oh_r = \nu\sqrt{\rho/a_i\gamma} = 0.0037$, indicate that viscous effects found in both systems will be small. For simplicity, we therefore assume inviscid flow in the present analysis.

Lastly, the possibility of Kelvin-Helmholtz (K-H) type of instability at the interface of the jet is considered. The critical wavenumber k_c of the K-H instability for the air-water interface of a sheet with finite thickness under the long wave approximation, derived from the dispersion relationship, is

$$k_c \approx \rho_g \left(v_g - v_l\right)^2 / \gamma = \rho_g \Delta v^2 / \gamma \tag{3.1}$$

where v_g, v_l and ρ_g are the fluid velocities for gas and liquid, and the density for gas, respectively. Using k_c the critical Weber number for the sheet can be calculated, $We_c = 2\pi\rho_l \Delta v^2/\gamma k_c \approx 1500$.

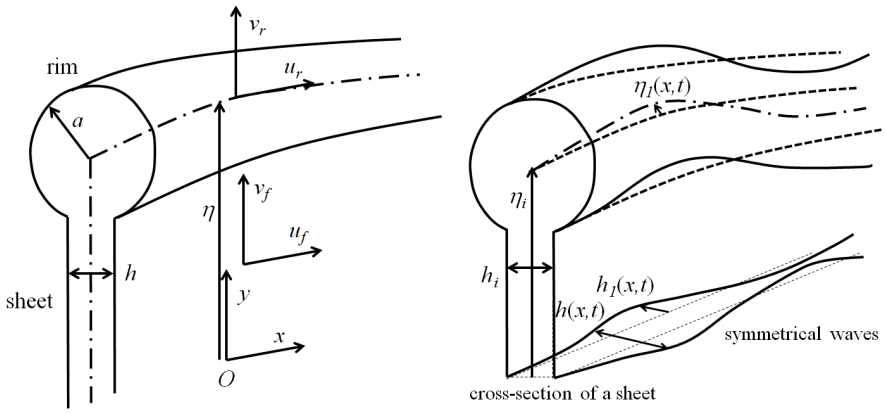

Figure 13. Coordinates and quantities in the rim-sheet system (left) and schematic representation of evolution of the perturbations (right).

Since the Weber number for the observed velocity and length scales in the present experiments is 56.2 we can safely ignore K-H instability in the following analysis.

4. Linear stability analysis

In this section a linear stability analysis of the transverse disturbances in rim-sheet system is performed. Based on the discussion of the previous section the fluid system will be treated as being incompressible, inviscid and irrotational with no tangential shear on the interface. We note that, by analogy with crown splashes [10,12], the capillary effect plays an important role in the axial deformation of the rim. In the flip-through case there is an additional transverse instability mode triggered through the undulations in the sheet and this may be coupled to the rim instability, leading to breakup of the rim-sheet system.

(a) Governing equation

The model of the rim-sheet system, presented here, is based on mass and momentum conservation for the both of the rim and fluid sheet of incompressible inviscid fluid, which is derived as an extension of Agbaglah et al. [12] . While the axial stretching of the rim, due to the radial crown expansion, decreases the amplitude of the perturbation [13], no such assumption can be made here as the planar sheet is initially ejected from the two-dimensional wave crest without any initial transverse stretching (Section 3 (f)).

The longitudinal oscillation of the sheet thickness, whose amplitude decreases with the distance to the rim, have also been observed during retraction for low Ohnesorge number flows [30,31]. As yet the presence of any longitudinal oscillation has not been confirmed in the present experiments, however, the generation mechanism for the observed transverse variations in sheet thickness may be interpreted as a re-orientation of capillary waves on a thin stretched sheet [20]. As this may modify the instability it should be included in the model of flip-through jets. Explicit mass and momentum exchanges between the rim and thinning sheet are also provided in the present model for describing the fully coupled dynamics of the rim and sheet system. Finally, since the length-scale characterising the deformation process is very small gravitational effects can be neglected.

The edge of the rising planar sheet, of uniform thickness $h(x,t)$, is bounded by a rim, with radius $a(x,t)$, located at a vertical elevation of $\eta(x,t)$. The horizontal and vertical fluid

velocities of the rim ($u_r(x,t)$, $v_r(x,t)$) and the film ($u_f(x,t)$, $v_f(x,t)$) are defined as shown in figure 13. The equations describing the mass and momentum conservation, based on a long-wave approximation, are:

$$\frac{\partial \eta}{\partial t} + u_r \frac{\partial \eta}{\partial x} = v_r \tag{4.1}$$

$$a\frac{\partial a}{\partial t} + \frac{a^2}{2}\frac{\partial u_r}{\partial x} + u_r a \frac{\partial a}{\partial x} = \frac{h}{2\pi}\left(v_f - v_r\right) \tag{4.2}$$

$$\rho\pi a^2\left(\frac{\partial u_r}{\partial t} + u_r\frac{\partial u_r}{\partial x}\right) = \pi\gamma\frac{\partial a}{\partial x} + \pi\gamma\frac{\partial}{\partial x}a^2\frac{\partial^2 a}{\partial x^2} + 2\gamma\frac{\partial \eta}{\partial x} + \rho h\left(v_f - v_r\right)\left(u_f - u_r\right) \tag{4.3}$$

$$\rho\pi a^2\left(\frac{\partial v_r}{\partial t} + u_r\frac{\partial v_r}{\partial x}\right) = 2\pi\gamma\left(\frac{\partial a}{\partial x}\frac{\partial \eta}{\partial x} + a\frac{\partial^2 \eta}{\partial x^2}\right) - 2\gamma + \rho h\left(v_f - v_r\right)^2 \tag{4.4}$$

where ρ is the density of the liquid and γ is the surface tension. The last terms of the right hand side of equations (4.2) – (4.4) present mass and momentum fluxes of liquid entering the rim from the sheet during the retraction [10].

Roisman et al. [10], Agbaglar et al. [12], all assume constant sheet thickness and velocity in the previous studies for their work on the crown splash, this is an appropriate assumption in describing the rim dynamics for spatially uniform and steady state of the sheet. Roisman [14] introduced a constant velocity gradient on the undeformable free sheet to model the effect of steady stretching on the rim instability. These previous studies examined a simplified rim model assuming that the rim does not have an inverse effect on flow in the film [32]. However, in the flip-through event, the presence of free rims may affect flow inside the sheet resulting in thinning deformation (see figure 11). In this case, the sheet dynamics should be solved simultaneously with the rim model (4.2) – (4.4) [32]. The mass and momentum conservation equations for a thin inviscid liquid sheet [19,32] are:

$$\frac{\partial h}{\partial t} + \frac{\partial hu}{\partial x} + \frac{\partial hv}{\partial y} = 0, \tag{4.5}$$

$$\frac{\partial hu}{\partial t} + \frac{\partial hu^2}{\partial x} + \frac{\partial huv}{\partial y} = \gamma\frac{\partial}{\partial x}h\frac{\partial^2 h}{\partial x^2}, \text{ and} \tag{4.6}$$

$$\frac{\partial hv}{\partial t} + \frac{\partial huv}{\partial x} + \frac{\partial hv^2}{\partial y} = 0. \tag{4.7}$$

In the flip-through case, variable transverse motion of a thinning sheet has been observed (see figure 11); consequently the sheet parameters $h(x,t)$, $u_f(x,t)$, $v_f(x,t)$ are functions of time as well as space (x) assuming vertically uniform flow in the sheet. As the mass flux from the sheet to the rim in the retraction (right hand side of equation (4.2)) decreases mass in the entire sheet, integrating (4.5) from $y = 0$ to η, the mass balance of the sheet yields

$$\eta\left(\frac{\partial h}{\partial t} + u_f\frac{\partial h}{\partial x} + h\frac{\partial u_f}{\partial x}\right) = -h\left(v_f - v_r\right). \tag{4.8}$$

In the same way, the momentum equations (4.6) and (4.7), vertically integrated from $y = 0$ to η, represent the mechanical balance of inertia of the sheet, surface tension and the momentum flux transfered from the sheet to the rim;

$$\rho h\eta\left(\frac{\partial u_f}{\partial t} + u_f\frac{\partial u_f}{\partial x}\right) = \gamma\frac{\partial}{\partial x}h\eta\frac{\partial^2 h}{\partial x^2} - \rho h\left(v_f - v_r\right)\left(u_f - u_r\right) \tag{4.9}$$

$$\rho h\eta\left(\frac{\partial v_f}{\partial t} + u_f\frac{\partial v_f}{\partial x}\right) = -\rho h\left(v_f - v_r\right)^2 \tag{4.10}$$

Equations (4.8) – (4.10) represent the capillary behaviour of the thinning sheet and are fully coupled with motion of the rim through flux exchanges of mass and momentum.

All the variables are nondimensionalised with the reference rim radius a_r and capillary time $\tau = \sqrt{\rho a_r^3/\gamma}$; $x^* = x/a_r$, $t^* = \sqrt{\gamma/\rho a_r^3}t$, $\eta^* = \eta/a_r$, $a^* = a/a_r$, $h^* = h/a_r$, $(u_r^*, v_r^*, u_f^*, v_f^*) = (u_r, v_r, u_f, v_f)\sqrt{\rho a_r/\gamma}$. The resulting dimensionless form of the above equation system is:

$$\frac{\partial \eta^*}{\partial t^*} + u_r^* \frac{\partial \eta^*}{\partial x^*} = v_r^* \tag{4.11}$$

$$a^* \frac{\partial a^*}{\partial t^*} + \frac{a^{*2}}{2}\frac{\partial u_r^*}{\partial x^*} + u_r^* a^* \frac{\partial a^*}{\partial x^*} = \frac{h^*}{2\pi}\left(v_f^* - v_r^*\right) \tag{4.12}$$

$$\pi a^{*2}\left(\frac{\partial u_r^*}{\partial t^*} + u_r^*\frac{\partial u_r^*}{\partial x^*}\right) = \frac{\partial a^*}{\partial x^*} + 2a^*\frac{\partial a^*}{\partial x^*}\frac{\partial^2 a^*}{\partial x^{*2}} + a^2\frac{\partial^3 a^*}{\partial x^{*3}} + \frac{2}{\pi}\frac{\partial \eta^*}{\partial x^*} + \frac{h^*}{\pi}\left(v_f^* - v_r^*\right)\left(u_f^* - u_r^*\right) \tag{4.13}$$

$$\pi a^{*2}\left(\frac{\partial v_r^*}{\partial t^*} + u_r^*\frac{\partial v_r^*}{\partial x^*}\right) = 2\left(\frac{\partial a^*}{\partial x^*}\frac{\partial \eta^*}{\partial x^*} + a^*\frac{\partial^2 \eta^*}{\partial x^{*2}}\right) - \frac{2}{\pi} + \frac{h^*}{\pi}\left(v_f^* - v_r^*\right)^2 \tag{4.14}$$

$$\eta^*\left(\frac{\partial h^*}{\partial t^*} + u_f^*\frac{\partial h^*}{\partial x^*} + h^*\frac{\partial u_f^*}{\partial x^*}\right) = -h^*\left(v_f^* - v_r^*\right) \tag{4.15}$$

$$\eta^*\left(\frac{\partial u_f^*}{\partial t^*} + u_f^*\frac{\partial u_f^*}{\partial x^*}\right) = \frac{1}{h^*}\frac{\partial h^*\eta^*}{\partial x^*}\frac{\partial^2 h^*}{\partial x^{*2}} - \eta^*\frac{\partial^3 h^*}{\partial x^{*3}} - \left(v_f^* - v_r^*\right)\left(u_f^* - u_r^*\right) \tag{4.16}$$

$$\eta^*\left(\frac{\partial v_f^*}{\partial t^*} + u_f^*\frac{\partial v_f^*}{\partial x^*}\right) = -\left(v_f^* - v_r^*\right)^2 \tag{4.17}$$

This set of the equations (4.11) – (4.17) describes fluid motion of the coupled rim-sheet system occurring in the flip-through process. They are used as the governing system of equations for the stability analysis. Henceforth, the superscript * is omitted for clarity.

(b) First order analysis

Initially a spatially independent flow which is uniform in the cross-sheet, x, direction is considered. Such a system has a uniform rim of radius, $a_0(t)$, rim location, $\eta_0(t)$, and rise velocity, $v_{r0}(t)$. It is attached to a uniform rising fluid sheet of thickness, $h_0(t)$, with velocity, $v_{f0}(t)$. Introducing small perturbations to the base state (see figure 13 right) gives $\eta(x,t) = \eta_0(t) + \eta_1(x,t)$, $a(x,t) = a_0(t) + a_1(x,t)$, $u_r(x,t) = u_{r1}(x,t)$, $v_r(x,t) = v_{r0}(t) + v_{r1}(x,t)$, $h(x,t) = h_0(t) + h_1(x,t)$, $u_f(x,t) = u_{f1}(x,t)$, and $v_f(x,t) = v_{f0}(t) + v_{f1}(x,t)$. It should be noted that in this case, where there is no transverse stretching and the impact is driven by a laterally uniform wave impact [4], there are no transverse base velocities for the rim or the sheet.

Substituting these variables into equations (4.11) – (4.17), the equation system for the first order perturbations is given by

$$\frac{\partial \eta_1}{\partial t} = v_{r1} \tag{4.18}$$

$$a_0\frac{\partial a_1}{\partial t} + a_1\frac{\partial a_0}{\partial t} + \frac{a_0^2}{2}\frac{\partial u_{r1}}{\partial x} = \frac{h_0}{2\pi}\left(v_{f1} - v_{r1}\right) + \frac{h_1}{2\pi}w_0 \tag{4.19}$$

$$a_0^2\frac{\partial u_{r1}}{\partial t} = \frac{\partial a_1}{\partial x} + a_0^2\frac{\partial^3 a_1}{\partial x^3} + \frac{2}{\pi}\frac{\partial \eta_1}{\partial x} + \frac{h_0}{\pi}w_0\left(u_{f1} - u_{r1}\right) \tag{4.20}$$

$$a_0^2\frac{\partial v_{r1}}{\partial t} + 2a_0a_1\frac{\partial v_{r0}}{\partial t} = 2a_0\frac{\partial^2 \eta_1}{\partial x^2} + 2\frac{h_0}{\pi}w_0\left(v_{f1} - v_{r1}\right) + \frac{h_1}{\pi}w_0^2 \tag{4.21}$$

$$\eta_1\frac{\partial h_0}{\partial t} + \eta_0\frac{\partial h_1}{\partial t} + \eta_0 h_0\frac{\partial u_{f1}}{\partial x} = -h_0\left(v_{f1} - v_{r1}\right) - h_1w_0 \tag{4.22}$$

$$\eta_0\frac{\partial u_{f1}}{\partial t} = \eta_0\frac{\partial^3 h_1}{\partial x^3} - w_0\left(u_{f1} - u_{r1}\right) \tag{4.23}$$

$$\eta_1\frac{\partial v_{f0}}{\partial t} + \eta_0\frac{\partial v_{f1}}{\partial t} = -2w_0\left(v_{f1} - v_{r1}\right) \tag{4.24}$$

where the relative vertical velocity for the base state of the rim and sheet motion are $w_0 = v_{f0} - v_{r0}$.

(c) Base flow

In the current analysis, the base solutions for the zeroth order variables at the initial state of the system are considered, assuming that base flow changes much more slowly than the perturbations. Consequently any temporal changes of the base state may be neglected. This, so-called, frozen approximation has often been used for linear stability analysis with time-variant base solutions [10,12]. In this case, equations (4.12) and (4.14) provides the relations of the initial rim radius a_i, rim velocity v_{ri} and sheet thickness h_i;

$$a_i^2 \dot{a_i}^2 = \frac{h_i^2}{4\pi^2} w_i^2 \tag{4.25}$$

$$a_i^2 \dot{v_{ri}} = -\frac{2}{\pi} + \frac{h_i}{\pi} w_i^2 \tag{4.26}$$

where w_i is the initial relative vertical velocity between v_{ri} and the sheet velocity v_{fi}. Using the above equations a relationship between the temporal change of the initial radius, $\dot{a_i}$, and the acceleration of the rim, $\dot{v_{ri}}$ can be found,

$$\dot{a_i}^2 = \frac{h_i}{4\pi} \left(\dot{v_{ri}} + \frac{2}{\pi a_i^2} \right). \tag{4.27}$$

In the same way the equations for the planar sheet may be derived from equations (4.15) and (4.17),

$$\dot{h_i}^2 = -\frac{h_i^2}{\eta_i} \dot{v_{fi}}. \tag{4.28}$$

As both $\dot{a_i}$ and $\dot{h_i}$ in equations (4.27) and (4.28) are determined from the initial constant parameters, a_i, h_i, η_i and $\dot{v_{ri}}$ (which are frozen), we have

$$\dot{v_{fi}} = -\frac{\pi}{h_i \eta_i} \left(a_i^2 \dot{v_{ri}} + \frac{2}{\pi} \right). \tag{4.29}$$

There are thus four frozen quantities a_i, h_i, $\dot{v_{ri}}$ and η_i which determine the base state of the system and which are used as parameters in the current analysis. The equation system (4.18) – (4.24) may be linearised with constant coefficients determined from the frozen parameters; $a_0 \approx a_i$, $h_0 \approx h_i$, $\eta_0 \approx \eta_i$, $v_{r0} \approx v_{ri}$, and $v_{f0} \approx v_{fi}$. It should be noted that the initial sheet length, η_i, is used as a parameter to describe the degree of the thinning effect owing to the stretching of the sheet rather than an exact measure of the initial sheet length.

(d) Solutions for perturbations

Introducing perturbational of the from

$$(\eta_1, a_1, v_{r1}, u_{r1}, h_1, v_{f1}, u_{f1}) = (\eta', a', v', u_r', h', v_f', u_f') e^{\sigma t + ikx} \tag{4.30}$$

where σ is the growth rate and k is the wavenumber, into (4.15) – (4.21) and solving gives:

$$\sigma \eta' - v_r' = 0 \tag{4.31}$$

$$a' (\sigma a_i + \dot{a_i}) + \frac{ik}{2} a_i^2 u_r' + \frac{h_i}{2\pi} v_r' - \frac{h_i}{2\pi} v_f' - \frac{w_i}{2\pi} h' = 0 \tag{4.32}$$

$$-\frac{2ik}{\pi} \eta' + ik \left(k^2 a_i^2 - 1 \right) a' + \left(\sigma a_i^2 + \frac{h_i w_i}{\pi} \right) u_r' - \frac{h_i w_i}{\pi} u_f' = 0 \tag{4.33}$$

$$2k^2 a_i \eta' + 2a_i \dot{v_{ri}} a' + \left(\sigma a_i^2 + \frac{2h_i w_i}{\pi} \right) v_r' - \frac{2h_i w_i}{\pi} v_f' - \frac{w_i^2}{\pi} h' = 0 \tag{4.34}$$

$$\dot{h_i} \eta' + (\sigma \eta_i + w_i) h' - h_i v_r' + h_i v_f' + ik \eta_i h_i u_f' = 0 \tag{4.35}$$

$$ik^3 \eta_i h' - w_i u_r' + (\sigma \eta_i + w_i) u_f' = 0 \tag{4.36}$$

$$\dot{v_{fi}}\eta' + (\sigma\eta_i + 2w_i)\, v_f' - 2w_i v_r' = 0. \tag{4.37}$$

Writing this system in matrix form, as

$$\mathbf{MA} = 0 \tag{4.38}$$

where

$$\mathbf{M} = \begin{pmatrix} \sigma & 0 & 0 & -1 & 0 & 0 & 0 \\ 0 & \sigma a_i + \dot{a_i} & ika_i^2/2 & h_i/2\pi & -w_i/2\pi & 0 & -h_i/2\pi \\ -2ik/\pi & ik\left(k^2a_i^2 - 1\right) & \sigma a_i^2 + h_i w_i/\pi & 0 & 0 & -h_i w_i/\pi & 0 \\ 2k^2 a_i & 2a_i\dot{v_{ri}} & 0 & \sigma a_i^2 + 2h_i w_i/\pi & -w_i/\pi & 0 & -2h_i w_i/\pi \\ \dot{h_i} & 0 & 0 & -h_i & \sigma\eta_i + w_i & ik\eta_i h_i & h_i \\ 0 & 0 & -w_i & 0 & ik^3\eta_i & \sigma\eta_i + w_i & 0 \\ \dot{v_{fi}} & 0 & 0 & -2w_i & 0 & 0 & \sigma\eta_i + 2w_i \end{pmatrix} \tag{4.39}$$

and

$$\mathbf{A} = \begin{pmatrix} \eta' & a' & u_r' & v_r' & h' & u_f' & v_f' \end{pmatrix}^T. \tag{4.40}$$

The derivatives of frozen parameters, $\dot{a_i}$, $\dot{h_i}$, $\dot{v_{ri}}$, $\dot{v_{fi}}$, in $\mathbf{M}$ can be expressed in terms of four parameters, η_i, a_i, h_i and w_i by using equations (4.27) – (4.29). The determinant of $\mathbf{M}$ must be zero to provide non-zero solutions;

$$\det(\mathbf{M}) = 0 \tag{4.41}$$

which leads to the eigenvalue equation described by a polynomial of degree 7. The perturbations grow in an unstable system when $\sigma > 0$, and attenuate when $\sigma < 0$. Multiple eigenvalues for an identical wavenumber may be obtained as solutions of the polynomial equation, depending on the initial frozen conditions of the system.

(e) Mechanical effects of a thinning film

Here we will discuss the effect of the thinning of the rising sheet on the dynamics of the rim-sheet system. Thinning drives the deformation process of the flip-through jets observed in figures 2 and 7, which is distinct from that observed in crown splashes.

The initial sheet length η_i can be considered as a parameter describing the degree of thinning, since the thickness of the whole sheet over length η_i is assumed to be uniformly reduced by the transfer of mass to the growing rim in the space independent base state. Thus, the thickness of a longer sheet undergoes less change for particular flux.

Assuming an infinitely long sheet, $\eta_i \gg h_0$, $\dot{h_i} \approx 0$, $\dot{v_{fi}} \approx 0$, equations (4.35) – (4.37) provide explicit relations for the perturbed quantities describing the rim and sheet;

$$h' = \frac{h_i w_i \eta_i^2 k^4}{(\sigma\eta_i + w_i)^4 + \eta_i k^3} u_r' \approx \frac{h_i w_i \eta_i^2 k^4}{(w_i + \eta_i\sigma)^4} u_r' + O(k^6) \tag{4.42}$$

$$u_f' = \frac{(\sigma\eta_i + w_i)^3 w_i}{(\sigma\eta_i + w_i)^4 + \eta_i k^3} u_r' \approx u_r' \frac{w_i}{w_i + \sigma\eta_i} + O(k^3) \tag{4.43}$$

$$v_f' = \frac{2w_i}{\sigma\eta_i + 2w_i} v_r' \tag{4.44}$$

The perturbed sheet quantities u_f', v_f' and h' become negligible in the case where $\sigma\eta_i \gg w_i$ for real positive σ, under these circumstances equations (4.31) – (4.34) reduce to the retraction based rim instability model of Agbaglah et al. [12].

In the special case of no momentum exchange between the rim and sheet, $w_i = 0$ (or $\dot{v_{fi}} = 0$), equations (4.22) – (4.24) are reduced to be a closed system for the sheet;

$$\frac{\partial h_1}{\partial t} + h_i \frac{\partial u_{f1}}{\partial x} = 0 \tag{4.45}$$

$$\frac{\partial u_{f1}}{\partial t} - \frac{\partial^3 h_1}{\partial x^3} = 0 \tag{4.46}$$

$$\frac{\partial v_{f1}}{\partial t} = 0 \tag{4.47}$$

While equation (4.47) indicates constant v_{f1}, equations (4.45) and (4.46) represent the dynamic beam equations;

$$\frac{\partial^2 h_1}{\partial t^2} + h_i \frac{\partial^4 h_1}{\partial x^4} = 0, \quad \frac{\partial^2 u_{f1}}{\partial t^2} + h_i \frac{\partial^4 u_{f1}}{\partial x^4} = 0, \tag{4.48}$$

which gives the dispersion relation $\omega^2 = h_i k^4$ for periodically oscillating capillary waves in x-direction. This solution corresponds to symmetrical waves on a thin sheet at the long-wave limit presented by Taylor [15], and that amplification of this type of capillary waves on a thinning sheet is described by Longuet-Higgins [20] (see also figure 13). Since there is no growth of the perturbation in this closed equation system for the sheet, no capillary contribution is provided to the rim dynamics in this case of no sheet stretch.

The eigenvalue equation for (4.31) – (4.34) at this limit shows an RT instability mode will be present, as follows:

$$a_i^2 \sigma_{RT}^4 + k^2 a_i / 2 \left(3 + k^2 a_i^2\right) \sigma_{RT}^2 + k^2 \left(2\dot{v_{ri}}/\pi - k^2 + k^4 a_i^2\right) = 0 \tag{4.49}$$

At the lowest wave number $k \to 0$, the positive eigenvalue is approximated by

$$\sigma_{RT} \equiv (2/\pi)^{1/4} \left(\pm\sqrt{-\dot{v_{ri}}}/a_i\right)^{1/2} k^{1/2} + O(k^{3/2}) \tag{4.50}$$

In the same way, for $\dot{v_{ri}} = 0$, the eigenvalue for RP mode as $k \to 0$ is approximated by

$$\sigma_{RP} \equiv (2a_i)^{-1/2} k + O(k^3) \tag{4.51}$$

In another limit $\eta_i \to 0$, the perturbed equation system (4.35) – (4.37) for the sheet is approximated by

$$\dot{h_i}\eta' + w_i h' + h_i \left(v_f' - v_r'\right) = 0 \tag{4.52}$$

$$w_i \left(u_f' - u_r'\right) = 0 \tag{4.53}$$

$$\dot{v_{fi}}\eta' + 2w_i \left(v_f' - v_r'\right) = 0 \tag{4.54}$$

Using these equations the perturbed thickness h' and the perturbed rim location η' can be related:

$$h' = \frac{h_i}{2\eta_i}\eta'. \tag{4.55}$$

With this relation, the rim-sheet system (4.31) – (4.37) is reduced to be the simple rim system with a thinning rate of the sheet $\dot{h_i}$ as a parameter of sheet stretch;

$$\left(\sigma a_i + \dot{a_i}\right) a' + \frac{ik}{2} a_i^2 u_r' + \dot{h_i}\eta' = 0 \tag{4.56}$$

$$-\frac{2ik}{\pi}\eta' + ik\left(k^2 a_i^2 - 1\right) a' + \sigma a_i^2 u_r' = 0 \tag{4.57}$$

$$\left(2k^2 a_i + \frac{h_i \dot{v_{fi}}}{\pi} + \sigma^2 a_i^2 + \frac{w_i \dot{h_i}}{2\pi}\right)\eta' + 2a_i \dot{v_{ri}} a' = 0 \tag{4.58}$$

Roisman et al. [33] introduced the local velocity gradient in the sheet $\partial v_{fi}/\partial y$ as a parameter describing rate of stretching into the model of the rim behaviour. In the current model, the gradient of sheet velocity is modelled as $\partial v_{fi}/\partial y \approx w_i/\eta_i = -\dot{h_i}/h_i$. The approximated equations

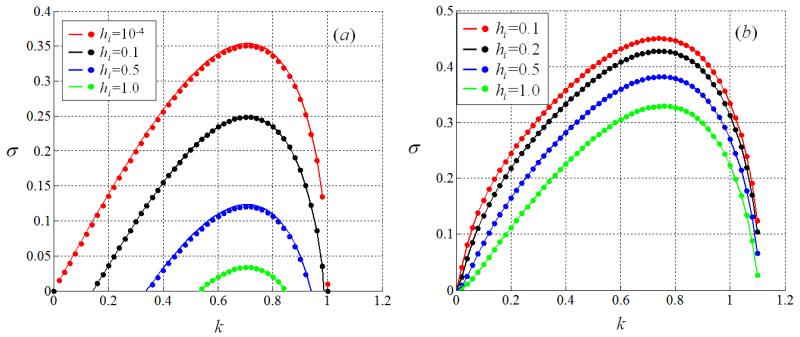

Figure 14. Growth rates of disturbances in the rim-sheet system as a function of the wavenumber in case $\eta_i = 1.0 \times 10^7$ and $a_i = 1.0$ (circle plot), and ones obtained by the rim model by Agbaglah et al. [12] (line plot); (a) $v_{ri}^{\cdot} = 0$, (b) $v_{ri}^{\cdot} = -0.5$.

(4.56) – (4.58) are consistent with the rim model of Roisman et al. [33] except the viscous shear force which is ignored in the current model.

In the present experimental results we find transitional sheet dynamics, where a thick sheet is ejected from the standing wave crest at high acceleration leading to rapid thinning as the sheet elongates longitudinally (see figure 11). In this case the transitional sheet lengths are modelled by the finite, moderate, range of η_i presenting a case which has not been analysed previously. For finite moderate sheet lengths (with both thinning and capillary effects) more complex mass and momentum exchanges between the rim and sheet induce multiple instability modes in the rim-sheet system.

(f) Results

The unstable modes of the coupled rim-sheet system are first compared with the rim instability of a crown splash. This comparison aims to identify the contributions of the sheet dynamics to the behaviour of the splashing jet system.

As already discussed, the current model with no thinning effect (i.e. $\eta_i \to \infty$) asymptotes to the rim of a crown splash [12]. The estimated growth rates with a very long fluid sheet, $\eta_i = 1.0 \times 10^7$, are completely consistent with the previous rim model for any initial rim conditions (see figure 14). The models provide the fundamental feature of the rim stability; growth rate with the most unstable wavenumber at $k \sim 0.7$, and destabilisation owing to decrease of h_i and $v_{ri}^{\cdot}$. As $h_i \to 0$ there can be no flux exchange of mass and momentum between the rim and the sheet, consequently the growth rate at the lowest wave number is proportional to k (equation (4.51)) and thus follows the RP mechanism in case $v_{ri}^{\cdot} = 0$ (figure 14 a). In the case of a thin sheet with negative acceleration $v_{ri}^{\cdot} = -0.5$(figure 14 b), the RT mode defines a steeper gradient of the growth rate at the lowest wave number (as $\sigma \propto \sqrt{k}$, see equation (4.50)). The agreement, in terms of the growth rates changes, between the present and previous study gives confidence that the presented rim-sheet model provides a reasonable description of both RP and RT mechanisms responsible for triggering the rim deformation.

Multiple instability modes emerge in competing mechanisms between capillary, retraction and sheet stretch mechanisms of the rim-sheet system, which are sensitive to the initial sheet thickness and rim acceleration. The largest and second largest eigenvalues for the case of $\eta_i = 10$ and $h_i = 0.1$ are shown in figure 15. While the wave number achieving the maximum growth rate ($k \sim 0.7$) is identical with those in figure 14, the unstable range extends into the low wave numbers. Roisman et al. [33] introduced the velocity gradient in the sheet, $S = \partial v_{fi}/\partial y$ as a

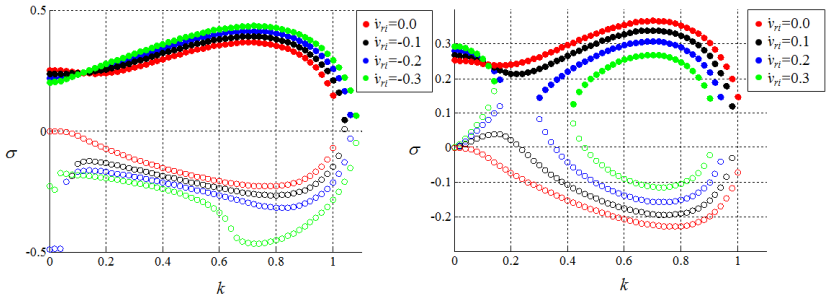

Figure 15. Growth rates of the rim-sheet system as a function of wave number for η=10, h_i=0.1, a_i=1.0; $\dot{v_{ri}} \leq 0$ (left), $\dot{v_{ri}} \geq 0$ (right). Filled and empty circles denote the first and second eigenvalues, respectively. η=10, h_i=0.1.

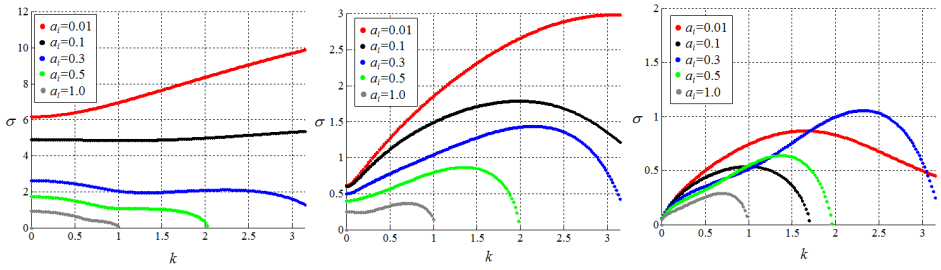

Figure 16. Dependencies of the relative rim size to the growth rates of disturbances as a function of wavenumber at $\dot{v_{ri}} = 0.0$ and $h_i = 0.1$; $\eta_i = 1.0$ (left), $\eta_i = 10.0$ (middle), $\eta_i = 100.0$ (right).

model of stretch effect to the rim stability of a crown splash. They found that destabilisation of the rim at low wave numbers in $0.1 \leq S \leq 5.0$, which is related to the weakening of the capillary effects, is less pronounced for long waves. As $\eta_i \to 0$ the present model approaches that of Roisman et al. (2007), see Section 4 (e). In figure 15 the velocity gradient $S \approx w_i/\eta_i$ lies in the range 0.32 to 0.54. This is within the range discussed by Roisman indicating that an identical mechanism may be responsible for destabilising the long-wave motions. This can be readily verified from the eigenvalues, σ_s, for equations (4.56) – (4.58) at $k = 0$ for the simplest case of $\dot{v_{ri}} = 0$; $\sigma_s = -\dot{a_i}/a_i$, and $\pm\sqrt{-2h_i\dot{v_{fi}} - \dot{h_i}v_{fi}}/\sqrt{2\pi}a_i$. The eigenvalue σ_s takes real positive value when the sheet thinning parameters $\dot{v_{fi}} < 0$ and $\dot{h_i} < 0$, which clearly indicates unstable laterally uniform response (as $k \to 0$) on the stretched sheet regardless of surface tension. It is also interesting to observe that while the first eigenvalues decrease with positive rim acceleration $\dot{v_{ri}}$ (figure 15 right), the second eigenvalues increases becoming positive, this results in two maximal growth rates at $k \sim 0.7$ for the first eigenvalue and in low wave numbers of $k < 0.5$ for the second one. This is relevant to the observed double spectrum peaks for the surface deformation (figure 10).

We will now consider the relative importance of the capillary and stretch effects during the retraction process on the stability of the rim-sheet system. While the long wave assumption is not valid for shorter scale fluctuations, $k > 1$, the growth rates of features of the rim and sheet associated with the largest eigenvalues (figure 16) may still be interpreted. For the case of high thinning rate of the sheet ($\eta_i = 1.0$), the systems with small rims, $a_i \leq 0.1$, are unstable over the whole range of wave numbers. Longuet-Higgins [20] showed the growth amplitude (ζ') of

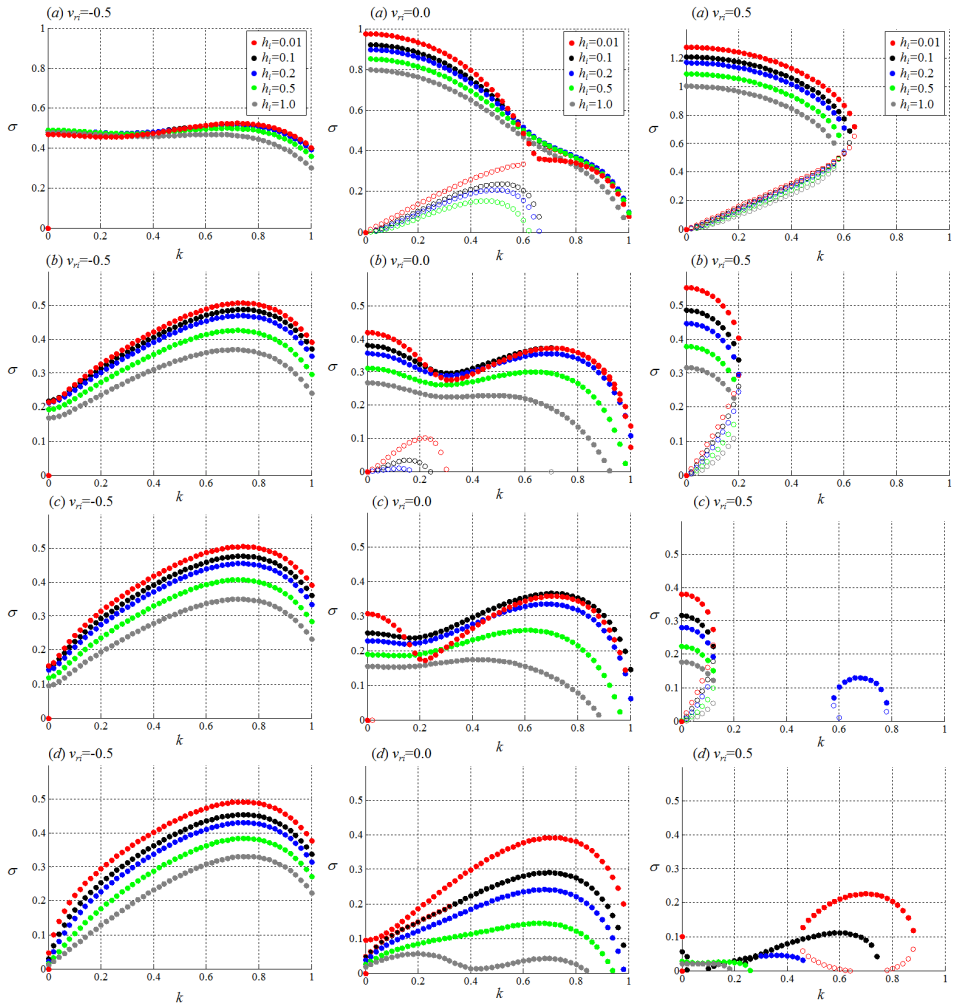

Figure 17. Growth rates of the rim-sheet system as a function of wave number for a_i=1.0; $v_{ri}^{\cdot} = -0.5$ (left), $v_{ri}^{\cdot} = 0.0$ (middle) and $v_{ri}^{\cdot} = 0.5$ (right), (*a*) $\eta_i = 1.0$, (*b*) $\eta_i = 5.0$, (*c*) $\eta_i = 10.0$ and (*d*) $\eta_i = 100.0$. Filled and empty circles denote the first and second eigenvalues, respectively.

perturbed surface displacements for symmetric long waves on a thin sheet, with thickness $2h$, stretched in the direction perpendicular to wave propagation on the basis of conservation of wave action is $\zeta'/h \propto h^{-1/4}$, indicating the relative amplitude grows on the stretched sheet regardless of wave number. We have also confirmed larger growth rates for thinner sheets at high rate of stretch. The sheet instability at the lowest wave number (amplifications of laterally uniform perturbations) is owing to unsteady effect of the thinning sheet as discussed above, which may results in rapid decrease of the perturbed sheet thickness along the neck of the lateral rim at the initial stage of flip-through in figure 7 (*a*) – (*c*) (see also figure 2). The increase of rim size a_i contributes to stabilise the system especially in high wave numbers, since the thinning effect relatively weakens (positive σ_s decreases with a_i) and thus the capillary effect accounts for the decay of the amplification rate in the regime of high wave numbers. As the sheet stretching attenuates, the systems for any rim size are stabilised over the entire wave numbers especially in the lowest wave numbers (see figure 16 middle and right).

Figure 17 shows the comparisons of the growth rates as functions of the sheet thickness, thinning rate and initial rim acceleration. In the case of high thinning rate, $\eta_i = 1.0$, the stretching effect on the sheet governs the stability of the system, resulting in significant growth rates over the entire long-wave regime, $0 \leq k \leq 1$, for (*a*) $v_{ri}^{\cdot} = -0.5$. It is interesting to find that the positive second eigenvalue appears at the peak wave number of $k \sim 0.5$ in (*a*) $v_{ri}^{\cdot} = 0.0$, indicating the emergence of another instability mode through coupled effects of the rim retraction and sheet stretch. The presence of real positive first and second eigenvalues indicates instability growths with two distinct time-scales for the perturbations at the identical wave number; that is, simultaneous emergence of faster and slower amplifications for two instability modes, which were never reported in the previous analyses for the crown splash. The two different time-scales characterising capillary motions of the sheet τ_{ch} and rim τ_{cr}, experimentally estimated in Section 3 (f), may be relevant to the multiple instability growth modes. In (*a*) $v_{ri}^{\cdot} = 0.5$, the second eigenvalue increases in proportion to wave number to be comparable with the first eigenvalue at $k \sim 0.6$ regardless of the sheet thickness, which also indicates the two instability modes simultaneously occurring in $0 < k < 0.6$, while no instability amplification is observed in $k > 0.6$. With increase of η_i for $v_{ri}^{\cdot} = -0.5$, as the capillary effect becomes dominant, the growth rate increases at $k \sim 0.7$ (see (*b*) and (*c*) $v_{ri}^{\cdot} = -0.5$). Two growth rate maxima are observed at the lowest wave number and at $k \sim 0.7$ for the neutral rim acceleration with η_i= 5.0 and 10.0 (see (*b*) and (*c*) $v_{ri}^{\cdot} = 0.0$), indicating simultaneous growth of the perturbed fluid motions at the two distinct length-scales. Since a thick sheet is insensitive to the capillary behaviour, the system is stabilised with increasing h_i for any cases, which may result in fundamental differences in the deformation of a thicker jet formed at pre-breaking impact (top panel of figure 8) from the flip-through case (figure 7). Figure 17 (*d*) $v_{ri}^{\cdot}$ = -0.5 shows the similar features of the instability growth to the case of no sheet stretch (figure 14 (*b*)), that is, RP and RT mechanisms destabilise the perturbed rim without available stretch effect. In positive rim acceleration, $v_{ri}^{\cdot} = 0.5$, the lowest wave number range containing two instability modes narrows with attenuation of the sheet stretch (increasing η_i). The wavenumber selections for these multiple instability modes, depending on transitions of the rim acceleration, sheet thickness and rim size, may occur during the flip-through event.

5. Mechanisms of transverse deformation of the flip-through jets

Although the frozen approximation used in the stability analysis cannot provide fully time-dependent stabilities throughout the event, the assumption of much faster growth of perturbations than the base state deformation of the jet still allows the use of the growth rates for analytical parameters corresponding to the experimental ones at sequential stages of the flip-through (as shown in figure 7). Figure 18 shows the observed spectra for the transverse deformation of the flip-through jets at the phase achieving the maximum value and the vertical distributions of the observed rim acceleration $v_{ri}^{\cdot}$, which are non-dimensionalised with the same characteristic length and time scales to the stability analysis (rim radius a_e and capillary time τ_{cr}, see Section 3 (f)). The wave numbers for the observed spectrum are explicitly compared with the ones for the analytical instability growth rates for the corresponding $v_{ri}^{\cdot}$. In figure 18 (right), the initial rim acceleration in the case of flip-through (x = 0.0 mm) decreases from $v_{ri}^{\cdot} \sim +0.5$ at z = 100 mm to $v_{ri}^{\cdot} \sim$ -0.5 at z = 200 mm owing to drag force and gravity. Therefore the rim accelerations, $v_{ri}^{\cdot}$= -0.5, 0.0 and 0.5, used in figure 17 cover the experimental range of the acceleration in the early stage of flip-through. In the flip-through case ($x = 0.0$ mm) of figure 18 (left), a single spectral peak initially appears at $k \sim 0.5$ (red broken line at z =100 mm), which subsequently evolves into a wider width spectrum.We find that the peak position, k_{p1}, moves to lower wave numbers with the measurement level z; $k_{p1} \sim 0.5$ at z= 100 mm, 0.4 at z= 150 mm, and 0.35 at z= 200 mm (see red arrows in figure 18 left), and that the peak width extends toward lower wave numbers. Another spectrum peak then emerges at $k_{p2} \sim$0.7 at z= 200 mm, forming double peak spectrum (red solid line). In the quasi-flip-through, the identical wavenumber shift ($k_{p1} \sim 0.35$ to 0.3, see black arrows) and the width extension for the lower wavenumber peak are observed while the peak position for

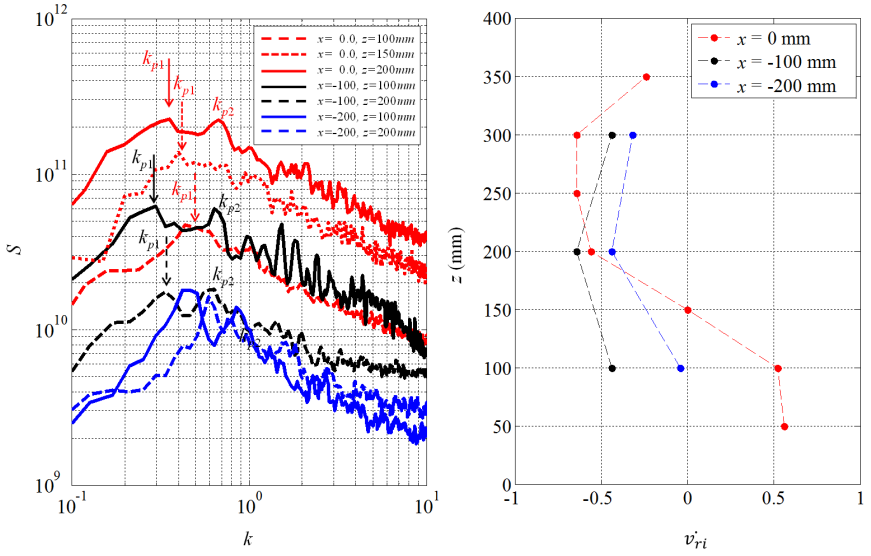

Figure 18. Dimensionless transverse wavenumber spectra of the integrated lengths for free-surfaces (left), and vertical distributions of dimensionless rim acceleration (right).

the higher one ($k_{p2} \sim 0.7$) is unchanged. These transitional features of the spectrum are relevant to the wavenumber selections during the transitional base state as discussed bellow.

In the flip-through, at the level $z \leq 100$ mm of figure 18 (right), the strong impact pressures rapidly accelerate the up rushing planar sheet. Since the stretching, and consequent thinning, of the sheet with positive acceleration ($v_{ri}^{\cdot} \sim 0.5$) governs the initial dynamics, the instability growth for the base state may correspond to (a) $v_{ri}^{\cdot} = 0.5$ in figure 17. The dominant instability modes occurring in the long-wave regime $k \leq 0.6$ may be associated with the observed prominent spectrum in $k \sim 0.4$ – 0.6 at z = 100 mm. It should be noted that the observed spectrum for the integrate length only reflects vertical displacement of the edges of jets not thickness (Section 3 (d)) while the analytical instability at the lowest numbers is relevant to long-scale variations of the sheet thickness. This may cause discrepancies between the observed spectrum and the analytical growth rates in low wave numbers. As the rim acceleration then decreases to zero at z =150 mm before achieving $v_{ri}^{\cdot} \sim -0.5$ at z =200 mm (figure 18 right), the sheet stretch attenuates in the transitional state corresponding to (a) – (c) $v_{ri}^{\cdot} = 0.0$ in figure 17. In these states with increasing η_i, the capillary instability with the growth at $k \sim 0.7$ becomes the dominant mechanism for the unstable rim-sheet behaviour, since the maximum growth rates at the lowest wave number decay as do the second eigenvalues in the middle range. We also find the wavenumber shift for the lower range of the maximal growth rates as the sheet stretch attenuates (η_i increases); the unstable range of $k < 0.65$ for $\eta_i = 1.0$, $k < 0.3$ for $\eta_i = 5.0$, and $k < 0.2$ for $\eta_i = 10.0$. The variations of the analytical unstable ranges suggest the attenuation of the sheet stretch in the decelerating jets can attain the wavenumber shift of the spectrum peak, k_{p1}, and the extension of the peak width toward low wave numbers as the jet rises. Finally, the RP and RT instabilities govern the perturbation growth in the retraction process under less effect of the sheet stretch (see figure 17 (c) or (d) $v_{ri}^{\cdot} = -0.5$), which achieves the most unstable wave number of $k \sim 0.7$ corresponding to the higher one of the peak wave numbers (k_{p2}) observed at z=200 mm in figure 18.

Although the current analysis does not explain large surface displacements beyond linear perturbations, the wavenumber selections for the instability modes responding to sequential base flow states consistently interpret a series of the deformations of the rim and the sheet at the

early stage in figure 7. Laterally uniform thinning on the sheet along the neck of the rim first emerges together with long-scale variations of the sheet thickness at about 1 – 2 cm intervals (stripe patterns of the image brightness) owing to the sheet stretch at phases (a) and (b), which corresponds to the initial instability growth in low wave numbers (figure 17 (a) $v_{ri}^{\cdot} = 0.5$). The fully thinned sheet is then partially ruptured with the identical wavelength for the undulating sheet thickness. The wavelength increases up to several cm in phases (c) and (d), owing to the wavenumber shift. The fingers are formed at the intervals of less than 1 cm, corresponding to the maximum capillary instability growth at $k \sim 0.7$, on the rim vertically undulating in syncronisation with the long-scale sheet deformations.

On the other hand, there are apparent differences in the dominant wave numbers for pre-breaking case (blue line in figure 18) and those in the flip-through event. This may be caused by the modification of unstable behaviours in the relatively thick, initial, jet (which limits capillary effects) and also through viscous effects at the wall contacting the liquid sheet. This maybe related to fingering instability of a spreading film [25].

6. Conclusions

The unstable behaviour and transverse deformation of violent up rushing fluid jets generated by a flip-trough event occurring when a steep breaking wave impacts on a vertical wall have been characterised using image analysis. Regular waves generated in a flume, shoal and then break on to a back-lit vertical wall, where the up rushing jet is captured with a high speed video camera.

Analysis of the video images shows that the up rushing jet is formed of a fluid sheet with a free rim at the leading edge, similar to that observed in the well-known crown splash. The rim undulates about the transverse axis to form organised regular cusps which are amplified and eventually form finger jets.

On the other hand, we have found inherent behaviours of the rim bounded sheet that are distinct from crown splashes. As the sheet extends from the standing wave crest it undergoes rapid stretching and consequently thinning, forming transverse undulations in sheet thickness. These undulations in the sheet are amplified by stretching and eventually rupture the sheet to form regular vertical ligaments. The finger shaped rim sections connected to these ligaments become detached from the main jet and break up to form spray. Computing the wave number spectra of the transverse displacements of the flip-through jet shows two dominant wave numbers.

A linear stability analysis of a model frozen, coupled, rim-sheet system has been performed. In this analysis the thinning sheet is modelled using a sheet length parameter to represent the stretching of the accelerating fluid sheet. A comparison of growth rates with respect to wave numbers between the present model (with no stretching) and the results presented by Agbaglah et al. [12], for rim instability under capillary and retraction dynamics, has been used to validate the model.

The relative mechanical roles played by the stretching and capillary effects acting on the rim on the stability of the fluid sheet are discussed in terms of linear perturbations. A system with a small rim and a highly stretched sheet is shown to be unstable over the entire long-wave range. According to Longuet-Higgins [20], the relative amplitude of symmetric capillary waves with respect to thickness of a thin sheet (without a rim) stretched in the direction perpendicular to propagation is proportional to -1/4 power of the thickness at the long-wave regime regardless of wave number; in other words, the perturbed surface displacements is amplified on a thinning sheet as a consequence of stretching, which supports the present analysis. The sheet stretch induces the instability associated with the lowest wave number, resulting in laterally uniform decrease in the sheet thickness along the rim, leading to rupture the sheet. As the rate of stretching attenuates, capillary processes begin to dominate the dynamics of the rim-sheet system and to stabilise the perturbed motion, especially at higher wave numbers, which asymptotes to RP and RT instability modes for the rim retraction.

Mechanisms to induce sequential transverse deformation of the rim-sheet system, leading to the double peak spectrum form of the surface displacement, are discussed in terms of instability growth defined by the analytical parameters corresponding to the experimental ones at sequential stages of the flip-through.

In the initial stage of flip-through, where sheet dynamics governs the stability of the rim-sheet system, two comparable positive eigenvalues appear in the low wave number range resulting in large-scale variations in sheet thickness along the lateral rim. The presence of real positive first and second eigenvalues indicates instabilities grow with two distinct time-scales at a given wave number. Therefore these perturbations are amplified at different velocities defined by the instability modes. As the rim decelerates owing to drag force and gravity and thus the stretch attenuates, two maxima in growth rate are observed at the lowest wave numbers and at $k \sim 0.7$. The low wave number range containing the growth rate maxima decreases with attenuation of the sheet stretch. This wavenumber shift in the unstable range has a role to change in wavelength of the sheet thickness and long-scale vertical displacement of the rim location. Finally the capillary instability with the most unstable wave number of $k \sim 0.7$ governs the system on the less stretch sheet with negative rim acceleration, which enhances short-scale rim deformations leading to finger formation. The sequential variations of the instantaneous instability growths for these multiple instability modes, depending on the sheet stretch, thickness, rim size and the accelerations, determines the integral features of the displacements of the ascending flip-through jets, resulting in the observed double peak spectrum.

Acknowledgements. The authors thank S. Ishizaki for his help in conducting experiments.

Funding statement. This research was supported by JSPS Grant-in-Aid for Scientific Research (15H04043).

References

1. M. J. Cooker and D. H. Peregrine 1990. A model for breaking wave impact pressure. *Proc. 22nd Int. Conf. on Coastal Engineering* 1473 – 1486.
2. M. J. Cooker and D. H. Peregrine 1995. Pressure-impulse theory for liquid impact problems. *Journal of Fluid Mechanics* **297**, 193 – 214.
3. C. Lugni, M. Brocchini and O. M. Faltinsen 2006. Wave impact loads: The role of the flip-through. *Physics of Fluids* **18**, 122101.
4. D. H. Peregrine 2003. Water-wave impact on walls. *Annu. Rev. Fluid Mech.* **35**, 23 – 43.
5. H. Bremose, D. H. Peregrine and G. N. Bullock 2009. Violent breaking wave impacts. Part 2: modelling the effect of air. *Journal of Fluid Mechanics* **641**, 389 – 430.
6. Y. Watanabe, H. Saeki and R. J. Hosking 2005. Three-dimensional vortex structures under breaking waves. *Journal of Fluid Mechanics* **545**, 291 – 328.
7. Y. Watanabe and N. Mori 2008. Infrared measurements of surface renewal and subsurface vortices in nearshore breaking waves. *Journal of Geophysical Research* **113**, doi:10.1029/2006JC003950.
8. A. Saruwatari, Y. Watanabe and D. M. Ingram 2009. Scarifying and fingering surfaces of plunging jets. *Coastal Engineering* **56**, 1109 – 1122.
9. J. Eggers and E. Villermaux 2008. Physics of liquid jets. *Rep. Prog. Phys.* **71**, 036601.
10. I. V. Roisman, K. Horvat and C. Tropea 2006. Spray impact: Rim transverse instability initiating fingering and splash, and description of a secondary spray. *Physics of Fluids* **18**, 102104.
11. R. Krechetnikov 2010. Stability of liquid sheet edges. *Physics of Fluids* **22**, 092101.
12. G. Agbaglah, C. Josserand and S. Zaleski 2013. Longitudinal instability of a liquid film. *Physics of Fluids* **25**, 022103.
13. Li V. Zhang, P. Brunet, J. Eggers and R. D. Deegan 2010. Wavelength selection in the crown splash. *Physics of Fluids* **22**, 122105-1 – 9.
14. I. V. Roisman 2010. On the instability of a free viscous rim. *Journal of Fluid Mechanics* **661**, 206 – 228.
15. G. I. Taylor 1959. The Dynamics of Thin Sheets of Fluid. II. Waves on Fluid Sheets. *Proceedings of the Royal Society of London. Series A, Mathematical and Physical Science* **253 (1274)**, 296 – 312.

16. G. I. Taylor 1959. The Dynamics of Thin Sheets of Fluid. III. Disintegration of Fluid Sheets. *Proceedings of the Royal Society of London. Series A, Mathematical and Physical Science* **253 (1274)**, 313 – 321.
17. N. Bremond and E. Villermaux 2006. Atomization by jet impact. *Journal of Fluid Mechanics* **546**, 273 – 306.
18. N. Bremond, C. Clanet and E. Villermaux 2007. Atomization of undulating liquid sheets. *Journal of Fluid Mechanics* **585**, 421 – 456.
19. A. L. Yarin and D. A. Weiss 1995. Impact of drop on solid surfaces: self-similar capillary waves, and splashing as a new type of kinematice discontinuity. *Journal of Fluid Mechanics* **283**, 141 – 173.
20. M. S. Longuet-Higgins 1995. On the disintegration of the jet in a plunging breaker. *Journal of Physical Oceanography* **25**, 2458 – 2462.
21. D. H. Peregrine 1981. The fascination of fluid mechanics. *Journal of Fluid Mechanics* **106**, 59 – 80.
22. I. V. Roisman and C. Tropea 2002. Impact of a drop onto a wetted wall: description of crown formation and propagation. *Journal of Fluid Mechanics* **472**, 373 – 397.
23. T. Bruce, J. Pearson and N. Allsop 2003. Hazards at coast and harbour seawalls-velocities and trajectories of violent ovetopping jets. *Proc. Int. Conf. on Coastal Engineering* 2216–2226.
24. H. Lamb 1945. Hydrodynamics, sixth edition. Dover Publication, p. 738.
25. S. M. Troian, E. Herbolzheimer, S. A. Safran and J. F. Joanny 1989. Figering instability of driven spreading film. *Europhys. Lett.* **10 (1)**, 25 – 30.
26. T. Chan and L. Vese 2001. An active contour model without edges. *IEEE Trans. on Image Processing* **10**, 266 – 277.
27. R. Rioboo, C. Tropea and M. Marengo 2001. Outcomes from a drop impact on solid surfaces. *Atomization and Sprays* **11**, 155 – 165.
28. I. Frankel and D. Weihs 1985. Stability of a capillary jet with linearly increasing axial velocity (with application to shaped charges). *Journal of Fluid Mechanics* **155**, 289 – 307.
29. C. Josserand and S. Zaleski 2003. Droplet splashing on a thin liquid film. *Physics of Fluids* **15**, 1650.
30. G. Sünderhauf, H. Raszillier and F. Durst 2002. The retraction of the edge of a planar liquid sheet. *Physics of Fluids* **14**, 198 – 208.
31. L. Gordillo, G. Agbaglah, L. Duchemin and C. Josserand 2011. Asymptotic behavior of a retracting two-dimensional fluid sheet. *Physics of Fluids* **23**, 122101.
32. A. L. Yarin 1993. Free liquid jets and films: hydrodynamics and rheology. Longman Scientific & Technical, p. 446.
33. I. V. Roisman, T. Gambaryan-Roisman, O. Kyiopoulos, P. Stephan and C. Tropea 2007. Breakup and atomization of a stretching crown. *Physical Review E* **18**, 102104.